† Supporting Information

Ultrathin dense LiF coverage coupled with a near-surface gradient fluorination lattice enables fast-charging long-life 4.6 V $LiCoO_2$

*Zhihong Bi [a, d, ‡], Zonglin Yi [b, ‡], Liangzhu Zhang [f], Gongrui Wang [a, e], Anping Zhang [a, d], Shihao Liao [a], Qinghe Zhao [c], Zhangquan Peng [j], Li Song [k], Yi Wang [a, d], Zhiwei Zhao [j], Shiqiang Wei [k], Wenguang Zhao [c], Xiaoyu Shi [a, e], Mingrun Li [a], Na Ta [a], Jinxing Mi [g], Shunning Li [c], Pratteek Das [a, e], Yi Cui [h, i], Chengmeng Chen *[, b], Feng Pan *[, c], and Zhong-Shuai Wu *[, a, e]*

[a] State Key Laboratory of Catalysis, Dalian Institute of Chemical Physics, Chinese Academy of Sciences, 457 Zhongshan Road, Dalian 116023, China

[b] CAS Key Laboratory of Carbon Materials, Institute of Coal Chemistry, Chinese Academy of Sciences, Taiyuan, 030001, China

[c] School of Advanced Materials, Peking University, Shenzhen Graduate School, Shenzhen 518055, China

[d] University of Chinese Academy of Sciences, 19 A Yuquan Road, Shijingshan District, Beijing 100049, China

[e] Dalian National Laboratory for Clean Energy, Chinese Academy of Sciences, 457 Zhongshan Road, Dalian 116023, China

[f] School of Materials Science and Engineering, East China University of Science and Technology, Shanghai 200237, China

[g] *State Key Joint Laboratory of Environment Simulation and Pollution Control, School of Environment, Tsinghua University, Beijing 100084, China*

[h] Vacuum Interconnected Nanotech Workstation, Suzhou Institute of Nano-Tech and Nano-Bionics, Chinese Academy of Sciences, 215123, Suzhou, China

[i] School of Nano Technology and Nano Bionics University of Science and Technology

of China, 230026, Hefei, China

[j] Laboratory of Advanced Spectro-Electrochemistry and Li-Ion Batteries, Dalian Institute of Chemical Physics, Chinese Academy of Sciences, Dalian 116023, China

[k] National Synchrotron Radiation Laboratory, CAS Center for Excellence in Nanoscience, University of Science and Technology of China, Hefei 230029, P. R. China

‡ *These authors contributed equally: Zhihong Bi, Zonglin Yi*

*Corresponding authors. E-mails: ccm@sxicc.ac.cn (C.M. Chen);

panfeng@pkusz.edu.cn (F. Pan); wuzs@dicp.ac.cn (Z.-S. Wu)

Methods

Materials synthesis

The commercial 4.45 V pristine LCO (named as P-LCO, purchased from JOHN LONG in Beijing) was uniformly mixed with $LiPF_6$-containing absolute ethanol solution at a mass ratio of 100:1 and continuously stirred until it was completely dried. Next, the composite electrodes were further dried in a blast drying oven at 90 °C for 6 h (named as LCO@LPF-90), and then transferred to a muffle furnace, which was heated to different temperatures of 400, 600 and 700 °C at a rate of 5 °C/min and subjected to thermal fluorination for 2 h. Finally, the fluorinated LCO samples were obtained, and correspondingly named as F-LCO-400, F-LCO, and F-LCO-700, respectively.

Materials characterizations

The morphologies, phases and crystallographic structures were characterized by XRD using a parallel-beam XRD instrument (Smartlab, Rigaku, with Cu Kα of wavelength 1.542 Å). The types and contents of doping elements of commercial LCO were determined by ICP-OES 7300DV (PerkinElmer). The surface chemistry was analyzed by XPS (Thermo Scientific Kα spectrometer). TEM samples were prepared by dual beam focused ion beam electron microscopy (FIB, Helios 450HP, FEI) using a 2-30 kV Ga ion beam. STEM (ARM200, JEOL; JEM-3200FS, JEOL; ARM300, JEOL) coupled with EELS/EDS were performed at different voltages (60 kV, 200 kV) to collect scanning transmission electron microscopy images for atomic and structural analysis, elemental and spectral analysis. The soft-XAS (SXAS) was performed at beamline 02B and XMCD Experimental Station (SSRF). Total electron yield (TEY)

mode (10 nm for probe depth) was used to collect the O K-edge SXAS spectra. ESR measurements were performed at 9.45 GHz with a Bruker spectrometer at the temperature of 100 K using an Oxford Instruments ESR 9 liquid nitrogen cryostat. TOF-SIMS analysis was performed by a TOF. SIMS 5 spectrometer (ION-TOF GmbH) to analyze the surface chemical structure and for depth profiling. All detected secondary ions of interest had a mass resolution of >5000 and possessed negative polarity. A pulsed 30 keV Bi^{1+} (20 ns) ion beam set at a high current mode was employed for depth profiling and a 500 eV Cs^{+} (negative) ion beam was utilized for the sputtering of the cycled electrodes with a typical sputtered area (300 μm × 300 μm). The typical analyzed area was 50 μm × 50 μm. The instruments used for in-situ differential electrochemical mass spectrometry (DEMS) experiments include commercial quadrupole mass spectrometer (Hiden HPR-20) equipped with turbo molecular pump (Pfeiffer vacuum) and rotary pump (Edwards vacuum), self-made cold trap, an electrochemical cell (EL CELL GmbH) and a digital mass flowmeter.

Electrochemical measurements

For the coin-type half cells, the cathode composite slurry was prepared by first mixing LCO active materials (80%), Ketjen black (10%, ECP600JD) and poly (vinylidene fluoride) (10%, PVDF) in N-methyl-2-pyrrolidone (NMP). Then, the composite slurry obtained was coated onto aluminum foil and then dried at 100 °C for 12 h under vacuum. The cathode mass loading was controlled at 2.5-3 mg cm^{-2}. The assembly of Li||LCO battery was completed using CR-2016 coin-type cells in an argon glove box (both of O_2 and H_2O contents below 0.1 ppm), including the cathode (diameter 12 mm),

polypropylene separator (diameter 19 mm, Celgard 2500), lithium metal foil (diameter 15.6 mm), electrolyte (LB-372: 1M $LiPF_6$ in fluoroethylene carbonate (FEC): methyl (2,2,2-trifluoroethyl) carbonate (FEMC)) purchased from Suzhou DoDo Chem Network. All the coin cells were evaluated using a Land CT3002A battery test system in a constant current mode between 3.0 and 4.6 V (*vs*. Li^+/Li) at 28 °C and 45 °C. The galvanostatic intermittent titration technique (GITT) was employed after 1 cycle by applying a pulse current of 0.1 C for 20 min with a time interval of 2 h in the voltage range of 3-4.6 V on a Land CT3002A battery test system. The cyclic voltammetry (CV) measurements, and electrochemical impedance spectroscopy (EIS) tests (100 kHz to 0.01 Hz, 5 mV) were measured on an electrochemical workstation (CHI760E, Shanghai Chenghua, China).

To evaluate room-temperature OER activity in aqueous solutions, electrocatalytic measurements were performed in a three-electrode cell using a glassy carbon rotating disk electrode (diameter: 3 mm) on an electrochemical workstation (CHI760E, Shanghai Chenghua, China). The Ag/AgCl was used as the reference electrode, and Pt wire was used as the counter electrode. 1 M KOH aqueous solution with continuous O_2 bubbling was used as the electrolyte. The remaining test steps were carried out as described in the previous literature.[23] Linear sweep voltammetry was conducted at 5 mV s^{-1}.

The pouch-type graphite||LCO full cells were completed in a dry room. The anode composite slurry was prepared by mixing graphite (94.3 wt%), acetylene black (1 wt%), styrene butadiene rubber (3.5 wt%, SBR) and carboxy methyl cellulose sodium (1.2

wt%, CMC) in deionized water. Then, the composite slurry obtained was coated onto the copper foil current collector and dried at 120 °C for 24 h under vacuum. The LCO cathode composite slurry was prepared by dispersing active materials (96%), ECP600JD (2%) and PVDF (2%) in NMP, followed by coating onto an Al foil current collector and drying at 120 °C for 24 h under vacuum. The graphite||LCO full cell consisted of LCO cathode, polypropylene separator, and graphite anode. LB-372 electrolyte consumption was about ~3.5g Ah^{-1}. The mass loading of the LCO electrode was about 12 mg cm^{-2} (on both sides of the Al foil current collector). The N/P ratio (negative to positive capacity ratio) was controlled around 1.05. For the formation process, the assembled pouch-type full cells were first put through two complete electrochemical cycles before the cycling specified in the main text. During this process, the pouch cells were first charged at 0.02 C for 2 h. After keeping for 5 min, the full cells were charged to 4.5 V at a constant current mode at 0.2 C and then constant voltage at 4.5 V until the current dropped to 0.02 C. Then, the pouch cells were discharged to 3.0 V at 0.2 C during the 1st discharge process. For the 2nd cycle, the pouch cells were charged to 3.85 V at 0.2 C and rested at 45 °C for 24 h to complete the formation process. The subsequent rate performance and cyclability by GCD profiles were conducted at a voltage window of 3.0–4.5 V. All pouch cell electrochemical tests were performed on a Land CT3001k battery test system.

Computational Details

Spin-polarized density functional theory (DFT) calculations were conducted by Vienna ab initio Simulation Package (VASP) 5.4.[1] The generalized gradient

approximation (GGA) and the Perdew−Burke−Ernzerhof (PBE) exchange−correlation function describe the exchange−correlation interaction.[2] The ion−electron interactions are described by the frozen-core projector augmented wave (PAW) method.[3] The GGA+U method was employed with Coulomb repulsion U = 3.91 eV.[4] The LCO bulk structure was constructed with dimensions 5.66 × 5.66 × 14.13. To investigate the effect of fluorination, one of the O atoms was substituted by F atom in bulk LCO. A 3 × 3 × 1 gamma-centered *k*-points grid was used for sampling the Brillouin zones in heterostructures, while 5 × 5 × 2 in bulk LCO. 9 × 9 × 3 gamma-centered k-points grids were used for self-consistent field (SCF) calculations in DFT. The plane wave basis energy cutoff was set to 550 eV. The convergence criteria are 0.04 eV/Å for maximum force, and 1×10^{-6} eV for energy changes. Electronic structure analysis was conducted with the help of Vaspkit package. The climbing image nudged elastic band (CI-NEB) method is conducted for simulating the migration of O atoms in pristine and F doped bulk LCO, with three climbing images between initial and final states generated through the transition state tools for VASP (VTST code).

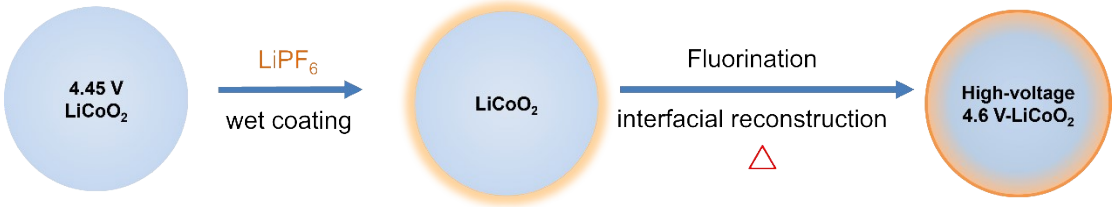

Supplementary Scheme 1| Fluorination interfacial reconstruction scheme of 4.6 V F-LCO derived from 4.45 V commercial P-LCO.

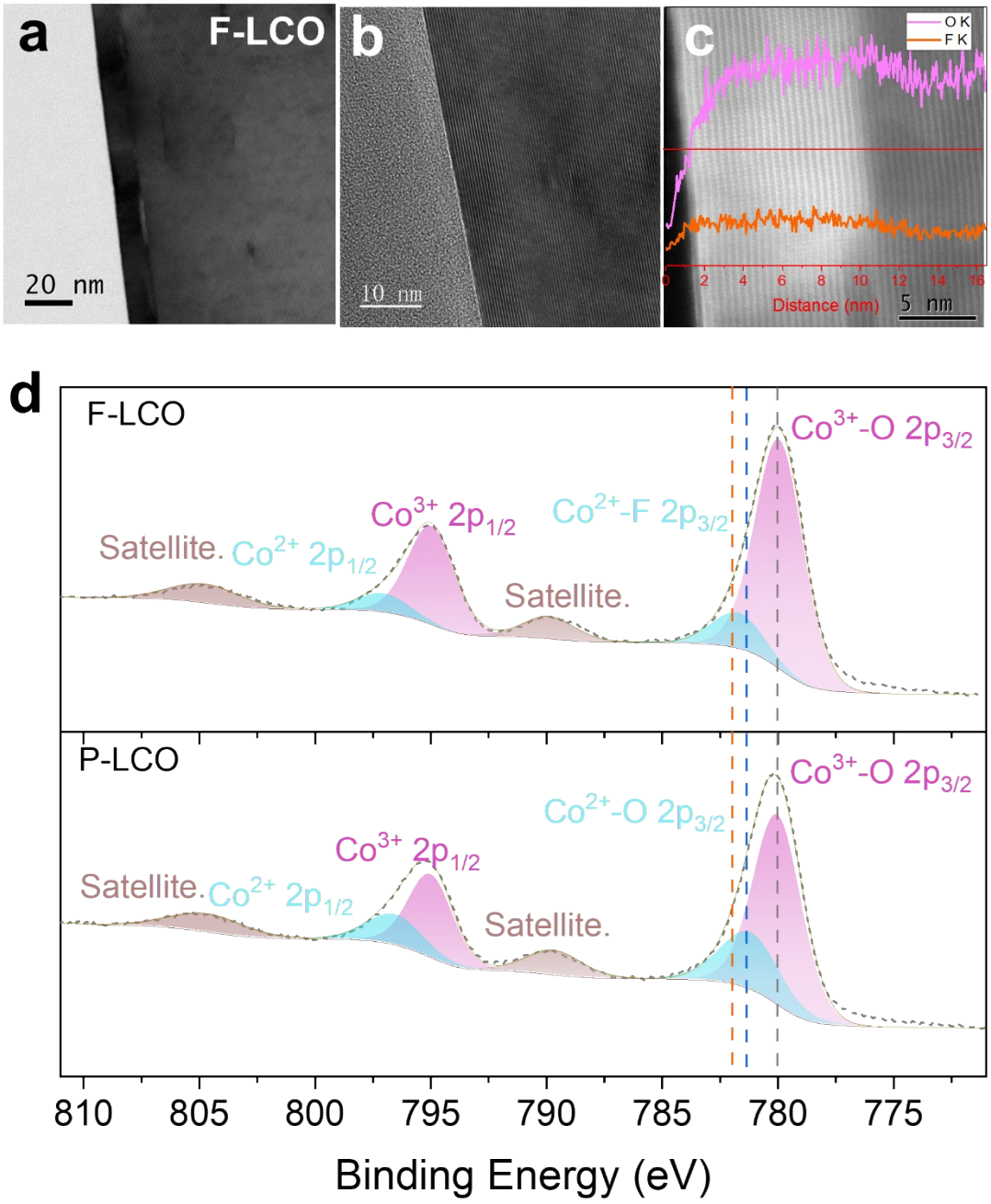

Supplementary Figure 1| (a,b) STEM-ABF images of F-LCO, and (c) high resolution STEM-HAADF image of F-LCO, with EDS Line scan signals of O K-edge and F K-edges across from the surface to the bulk phase of F-LCO particle. (d) Co 2p XPS spectra from F-LCO and P-LCO, after surface fluorination, the position of Co^{2+} shifts to a high binding energy and transforms from Co-O to Co-F.

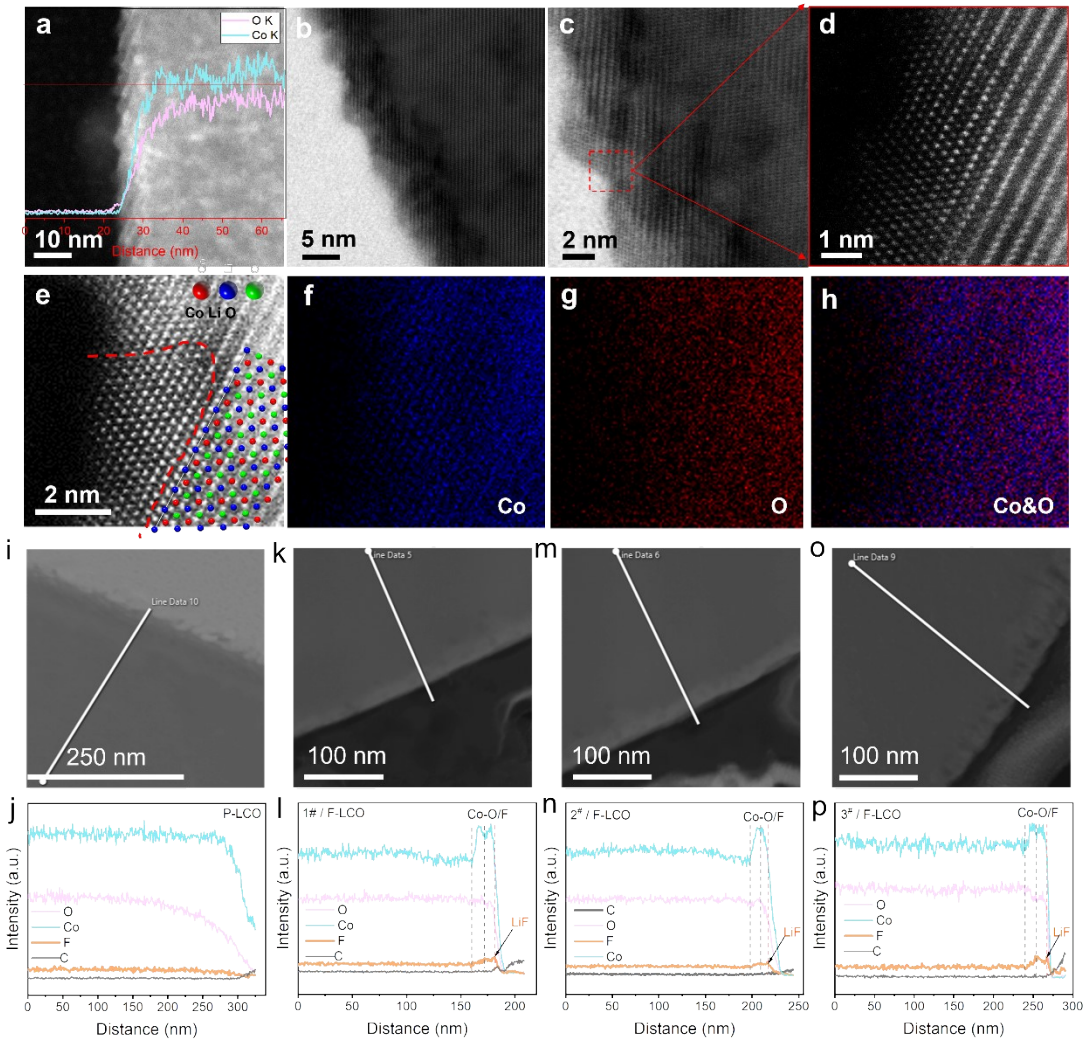

Supplementary Figure 2| (a) STEM-HAADF image of P-LCO (with EDS mapping area in the STEM-HAADF image, and line scan signal counts across from the surface to the bulk phase of LCO particle). (b-d) High resolution STEM-HAADF images of P-LCO by spherical aberration corrected transmission electron microscope at different nanoscale. (e) Atomic-resolution STEM HAADF image of subsurface for P-LCO at 2 nm scale and the ordered atomic structure model features of (003) planes corresponding to the image (d) (the zone axis is [-2 -1 0]). (f-h) EELS mapping of (f) Co and (g) O and (h) their overlay from image (e). (i-p) STEM-HAADF image and corresponding EDS line scan signal counts across from the surface to the bulk phase of LCO particles,

(i-j) P-LCO, and (k-p) F-LCO.

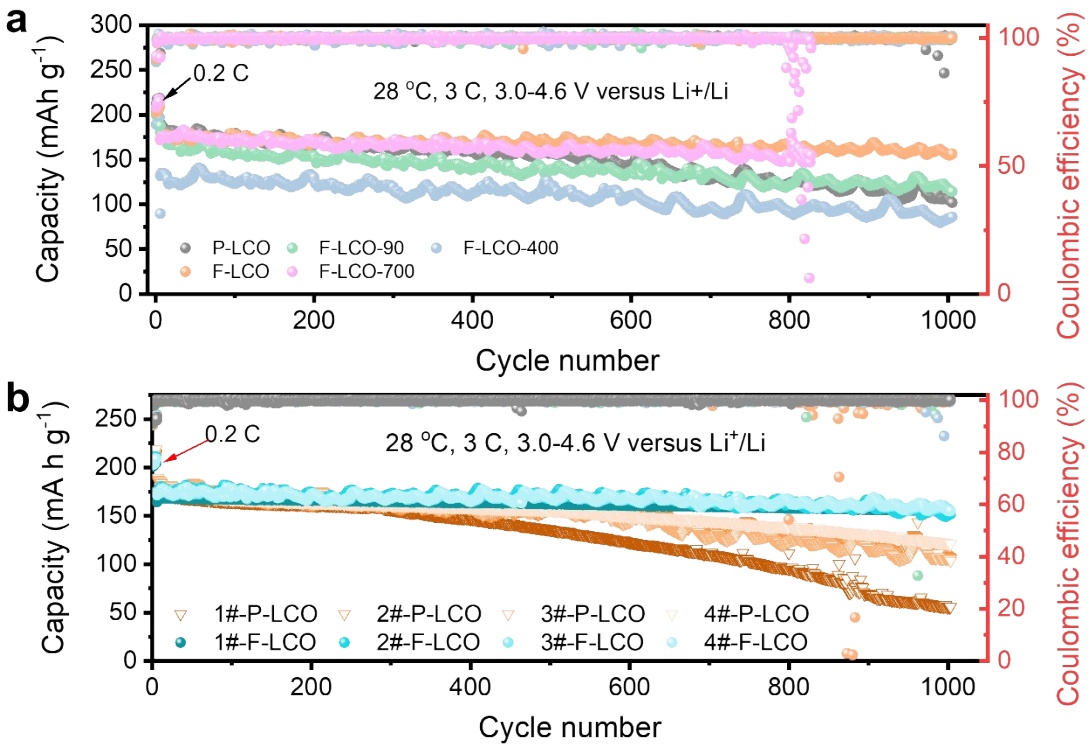

Supplementary Figure 3| (a) Long-term cycling performance of P-LCO, F-LCO and F-LCO-90, F-LCO-400, and F-LCO-700 obtained at a high rate of 3 C in the voltage of 3.0-4.6 V (*vs*. Li^+/Li). (b) Long-term cycling performance of multiple different P-LCO and F-LCO cathodes at 3C.

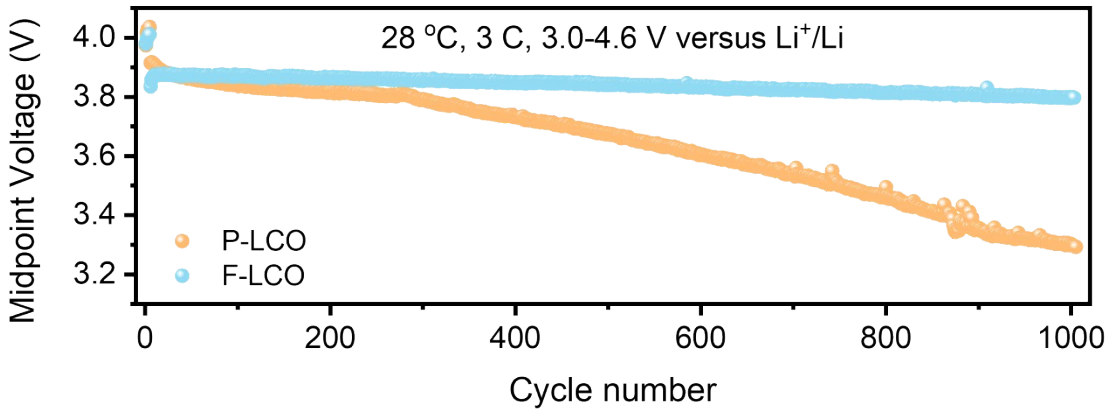

Supplementary Figure 4| The corresponding discharge midpoint voltages of F-LCO and P-LCO for 1000 cycles obtained at 3 C.

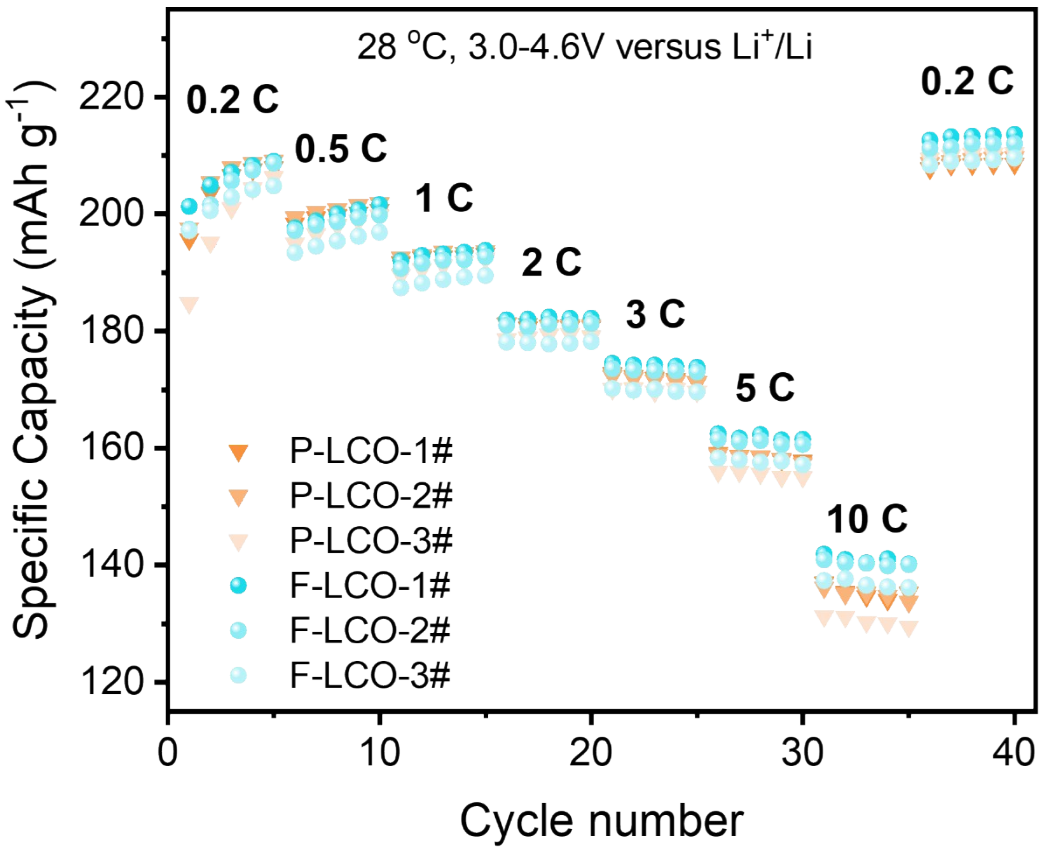

Supplementary Figure 5| Rate performance of F-LCO and P-LCO between 3.0 and 4.6 V in multiple half cells.

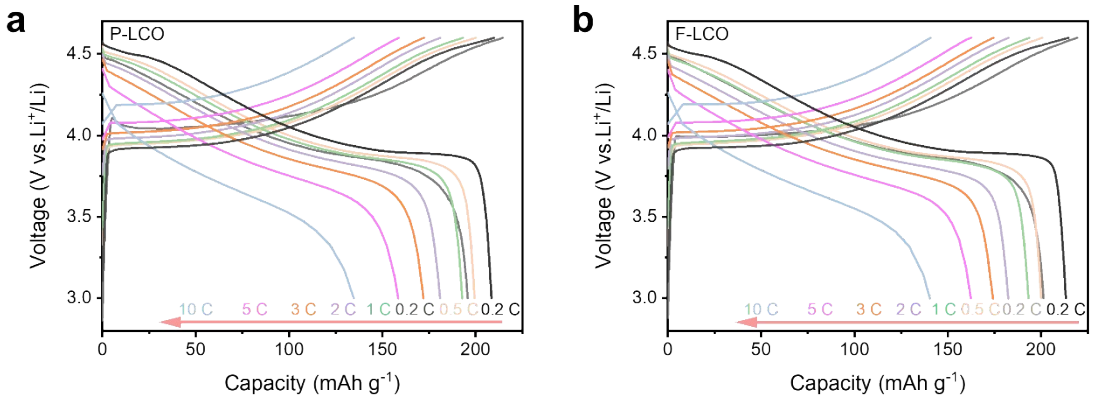

Supplementary Figure 6| The GCD profiles of (a) P-LCO and (b) F-LCO at different rates between 3.0 and 4.6 V.

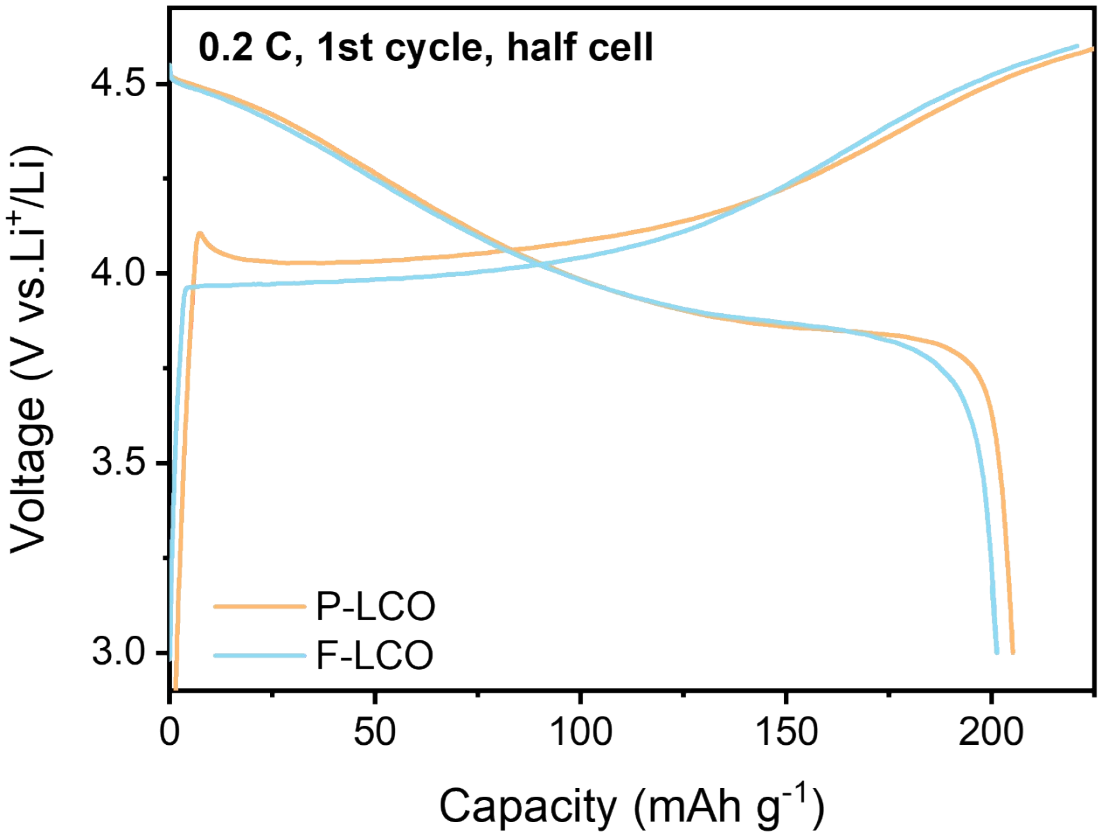

Supplementary Figure 7| The GCD profiles of F-LCO and P-LCO cathodes tested at 0.2 C within 3.0-4.6 V in half-cells.

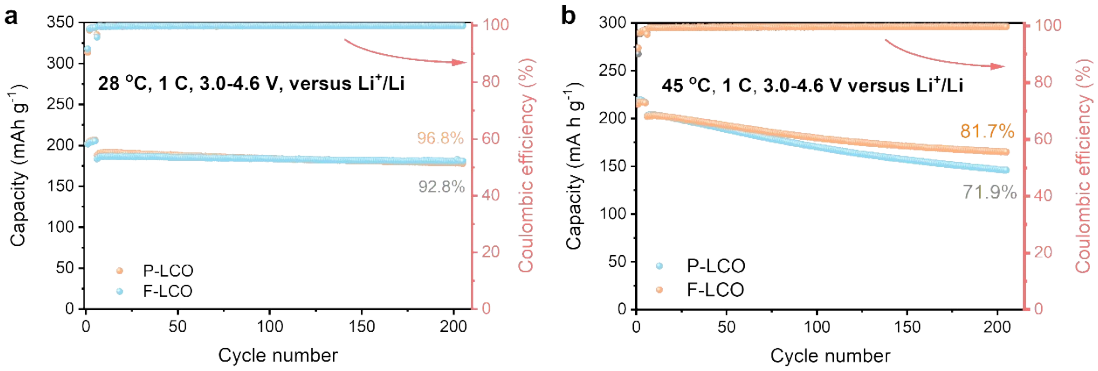

Supplementary Figure 8| Cycling performance of F-LCO and P-LCO at 1 C under (a) 28 ºC and (b) 45 ºC.

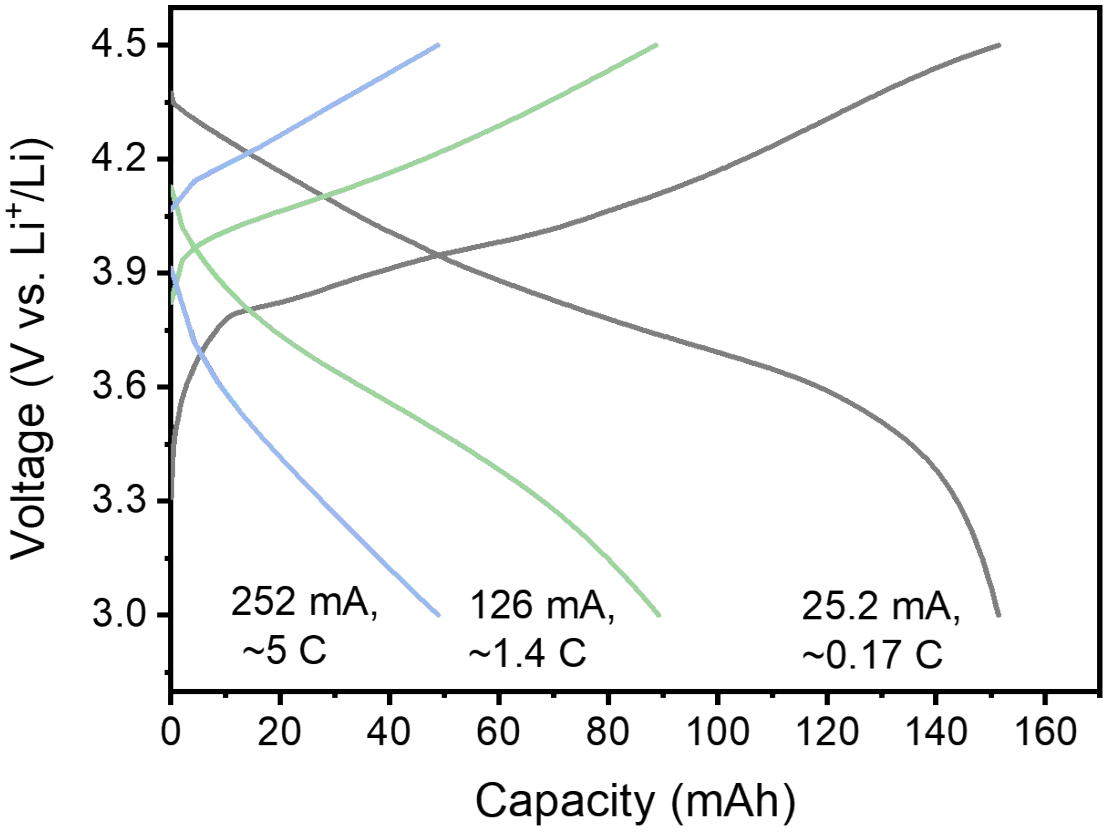

Supplementary Figure 9| The GCD profiles of graphite||F-LCO pouch-type full cells measured at 0.1 C, 0.5 C, and 1 C within 3.0-4.5 V.

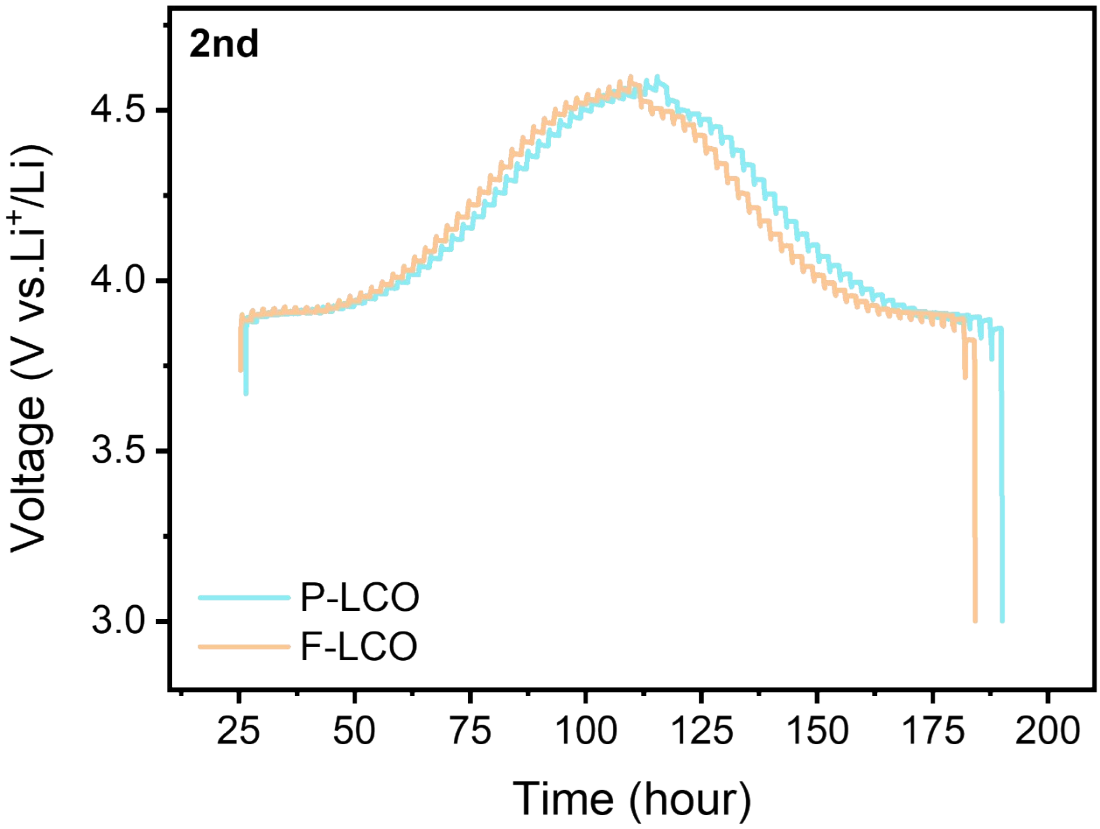

Supplementary Figure 10| The GITT curves of P-LCO and F-LCO at 0.2 C in the voltage of 3.0-4.6 V.

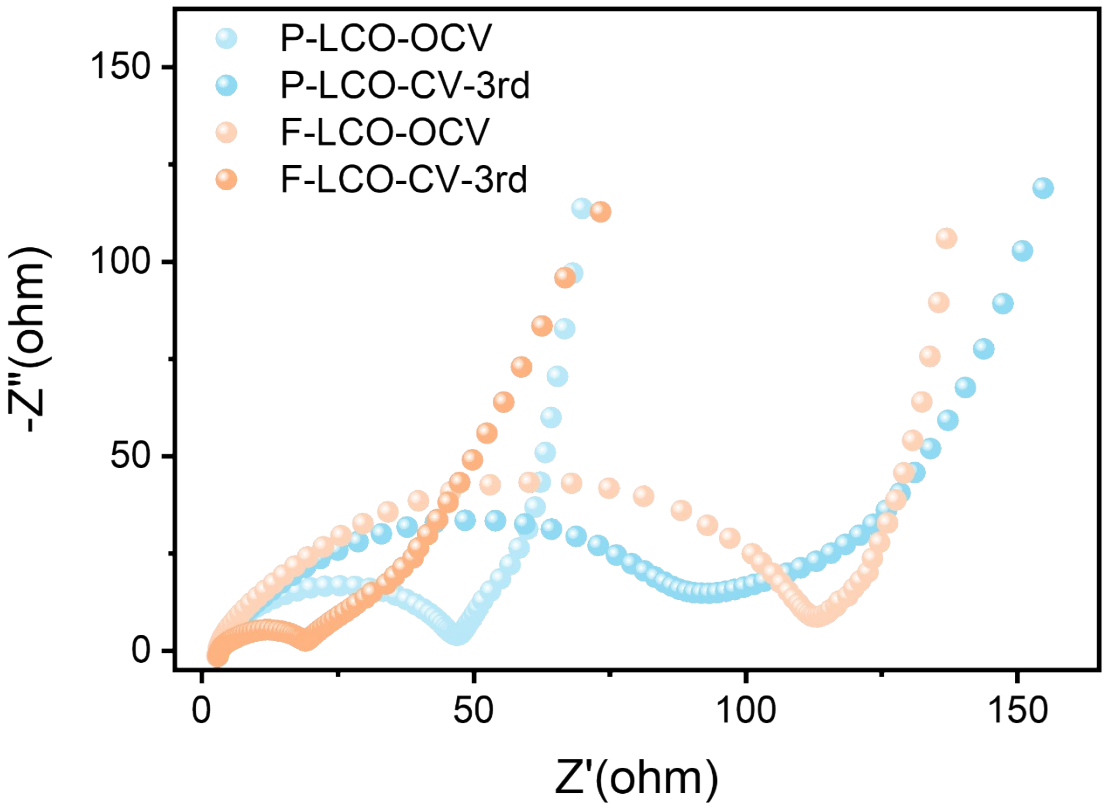

Supplementary Figure 11| Nyquist plots of Li||LCO (*vs.* Li^+/Li) batteries for P-LCO and F-LCO at open circuit voltage (OCV) and after three cycles CV curves at 0.1 m Vs^{-1}.

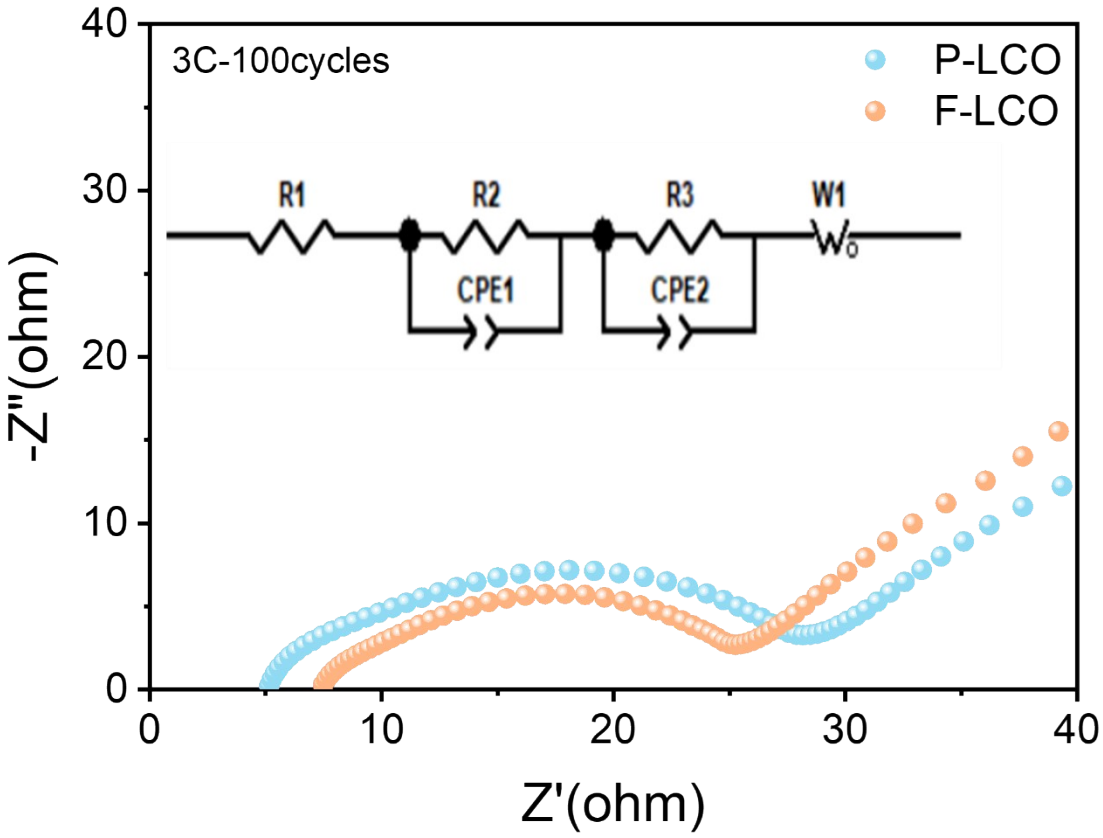

Supplementary Figure 12| Nyquist plots of F-LCO and P-LCO after 100 cycles at 3 C.

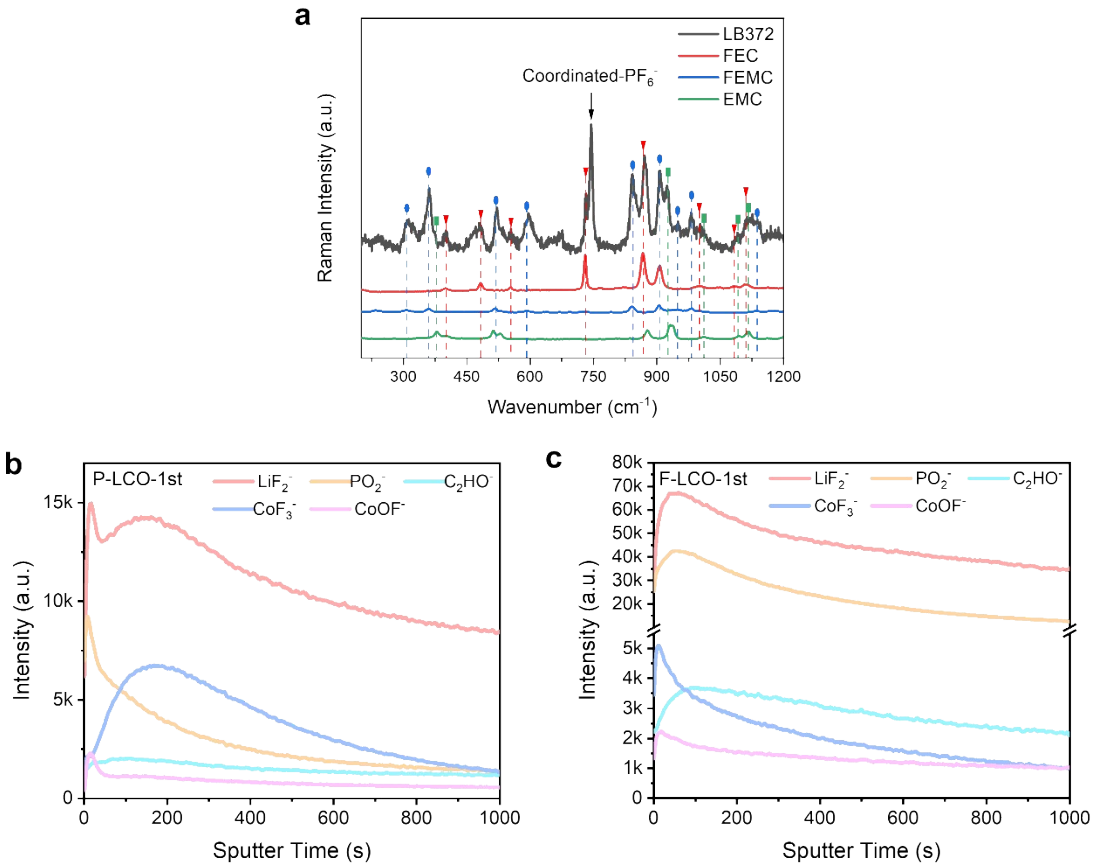

Supplementary Figure 13| (a) Raman characterization of electrolyte composition. (b,c) TOF-SIMS depth profiles of interphase fragments acquired on the cycled (b) P-LCO and (c) F-LCO cathodes, illustrating the different composition of CEI layer, retrieved from coin-type half cells after the 1st cycle at 0.2 C.

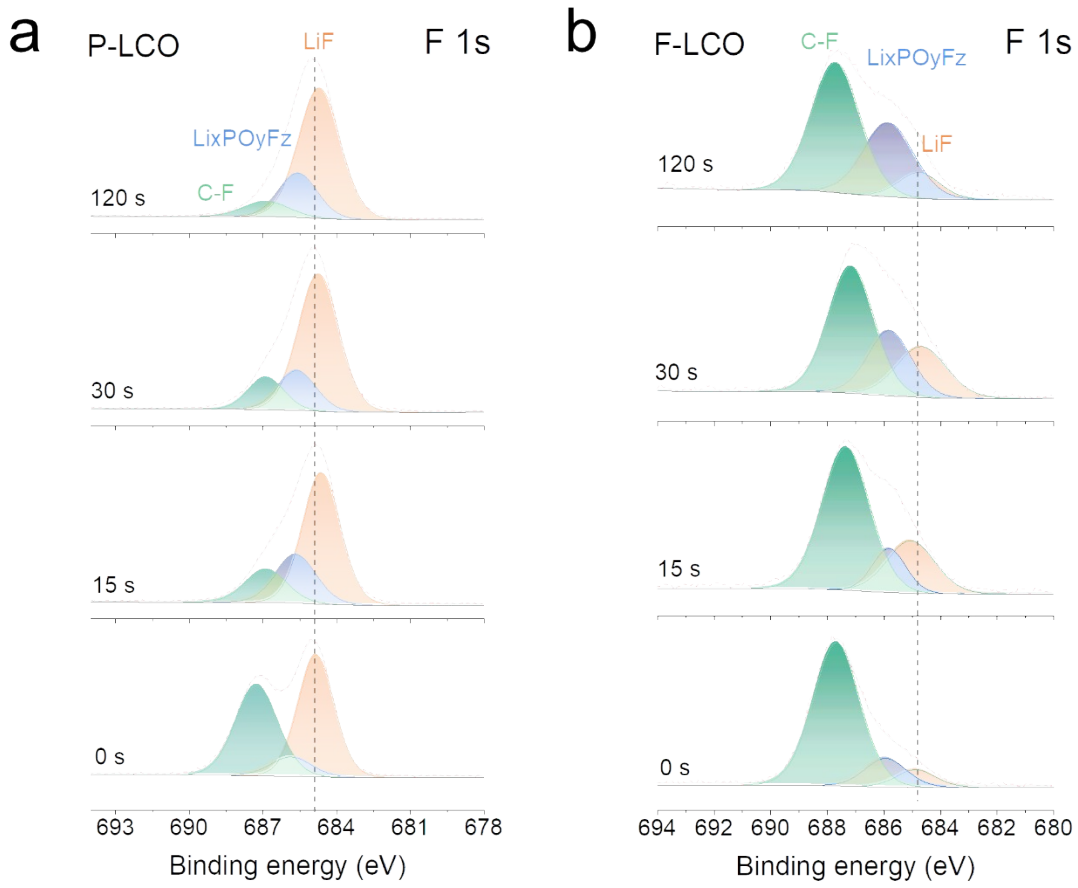

Supplementary Figure 14| The F 1s XPS spectra for analyzing the chemical composition of cycled (a) P-LCO and (b) F-LCO cathodes after 1000 cycles. The significant LiF generated by $LiPF_6$ decomposition suggests that P-LCO interfacial instability triggers a sustained side reaction, while F-LCO exhibits a relatively stable low LiF signal.

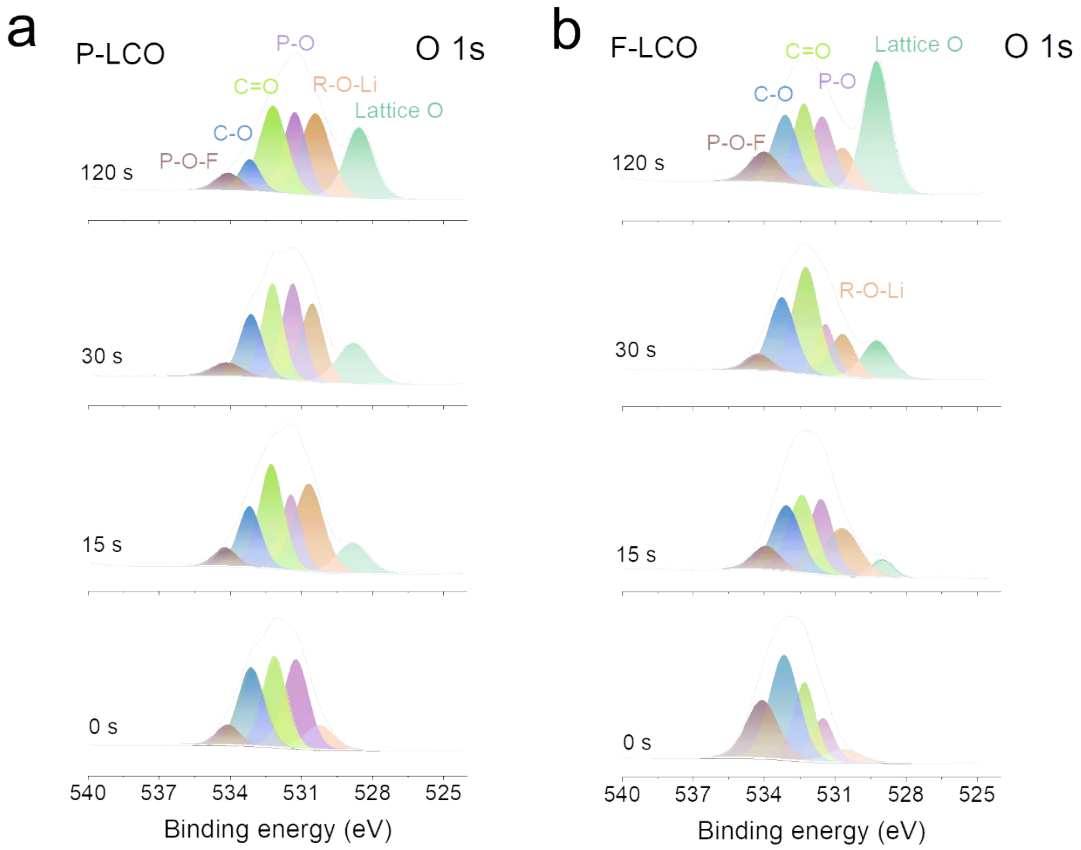

Supplementary Figure 15| The O 1s XPS spectra for chemical composition analysis of the cycled (a) P-LCO and (b) F-LCO cathodes after 1000 cycles. The relative strength of the lattice oxygen signal at 120 s qualitatively shows that the P-LCO surface produces the thicker CEI layer than that of F-LCO.

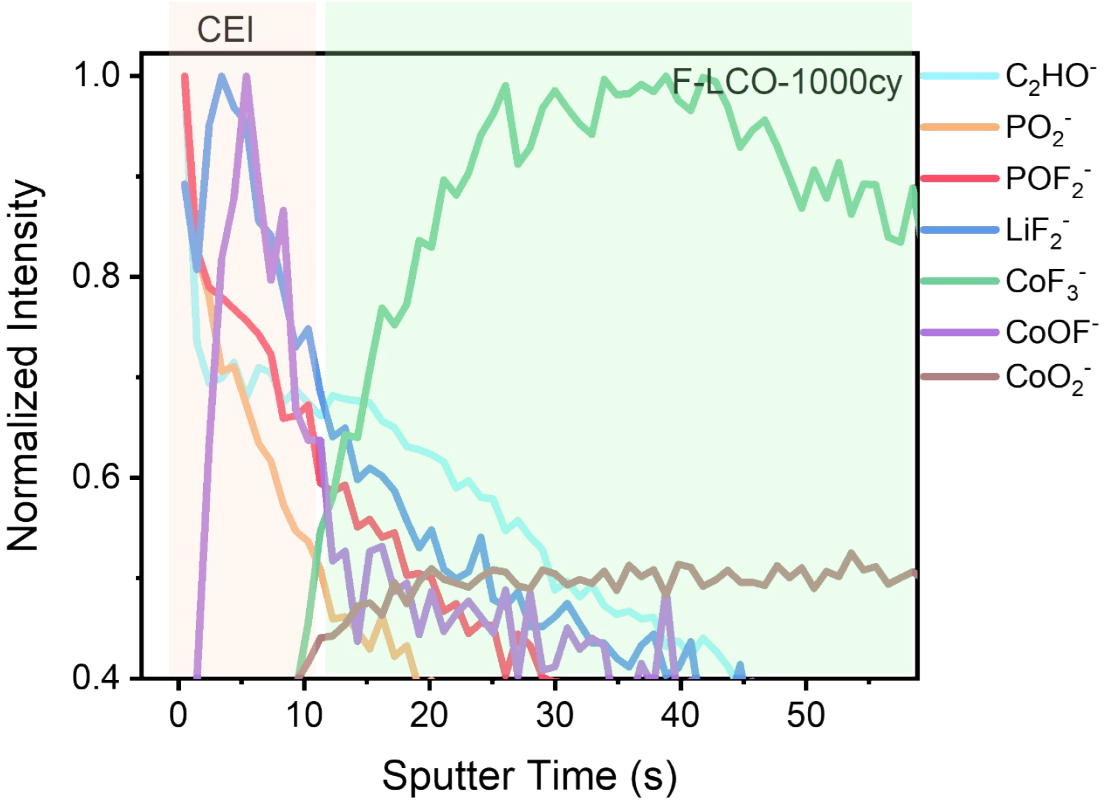

Supplementary Figure 16| Normalized TOF-SIMS depth profiles of representative species on cycled F-LCO cathodes after 1000 cycles. The maximum normalized intensity of $CoOF^-$ lies between LiF_2^- and CoF_3^-, indicating the formation of a Co-O-F-heterogeneous bonding interface between LiF and LCO.

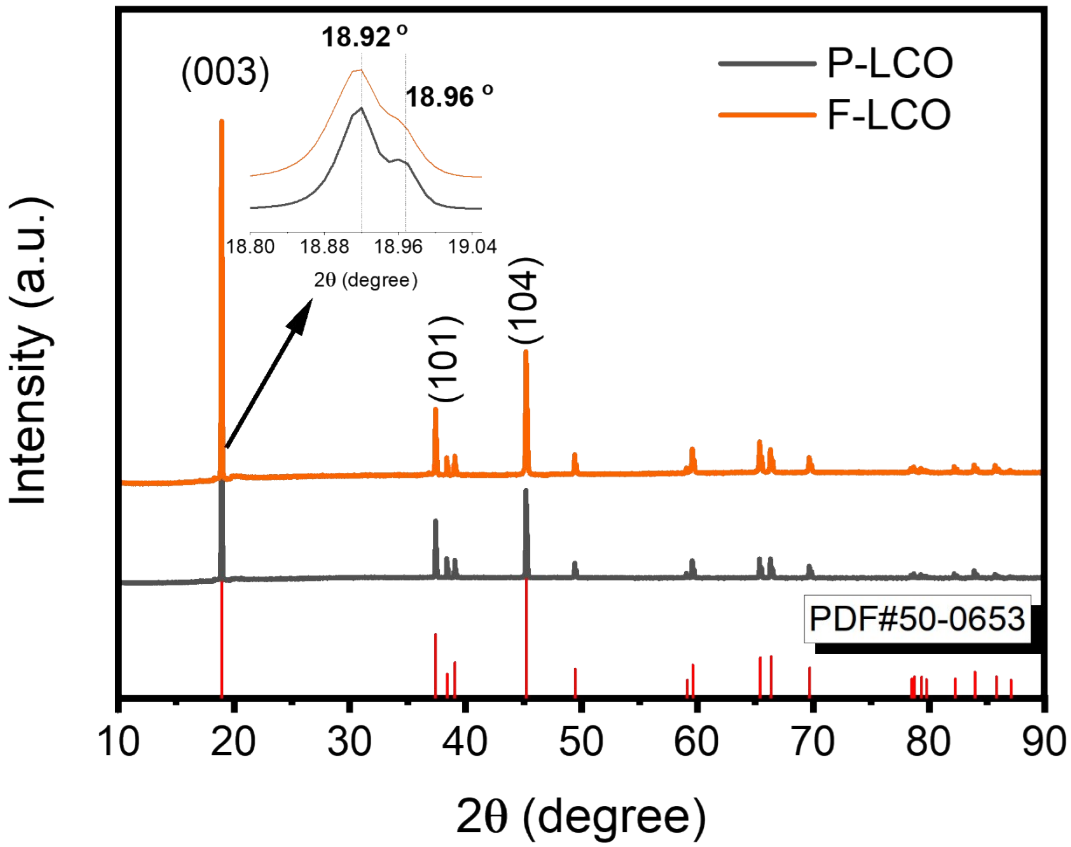

Supplementary Figure 17| The XRD patterns of P-LCO and F-LCO.

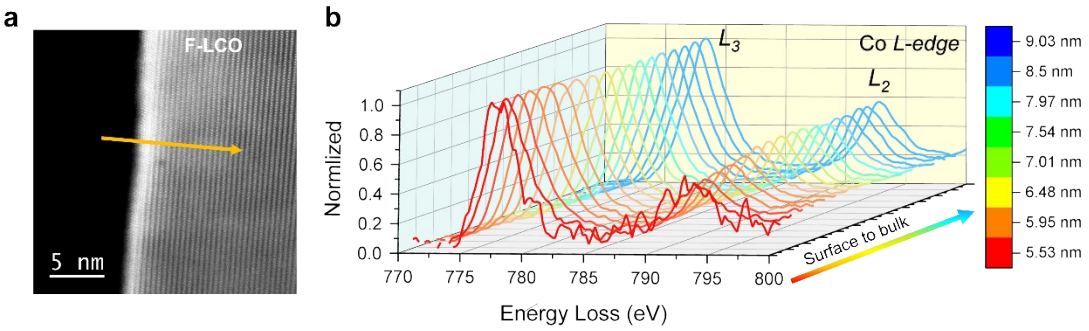

Supplementary Figure 18| (a) EELS line scan for F-LCO under high magnification STEM-HAADF mode and (b) 3D EELS spectra of Co *L*-edges after being normalized to L_3-edge.

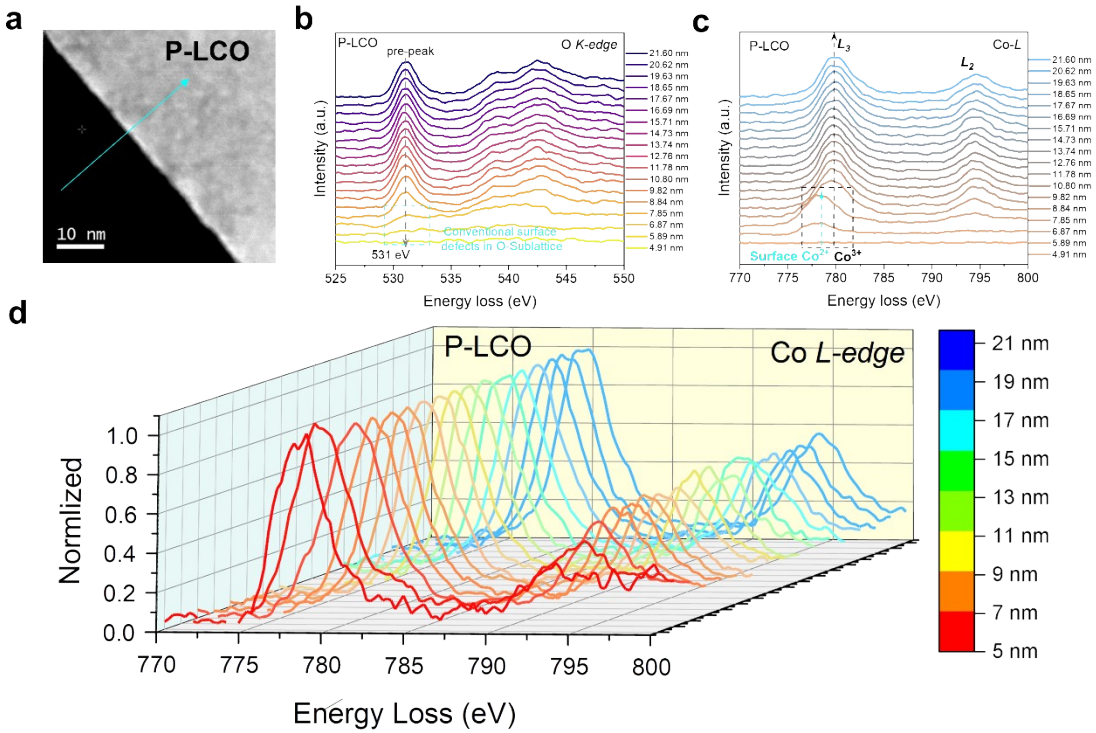

Supplementary Figure 19| (a) STEM-HAADF image of P-LCO particle after FIB fabrication. The lines in the figure represent the EELS line-scan. (b,c) EELS spectra of O K-edges in (b) and Co *L*-edges in (c) collected from P-LCO particle. (d) 3D EELS spectra of Co *L*-edges after being normalized to L_3-edge of P-LCO particle.

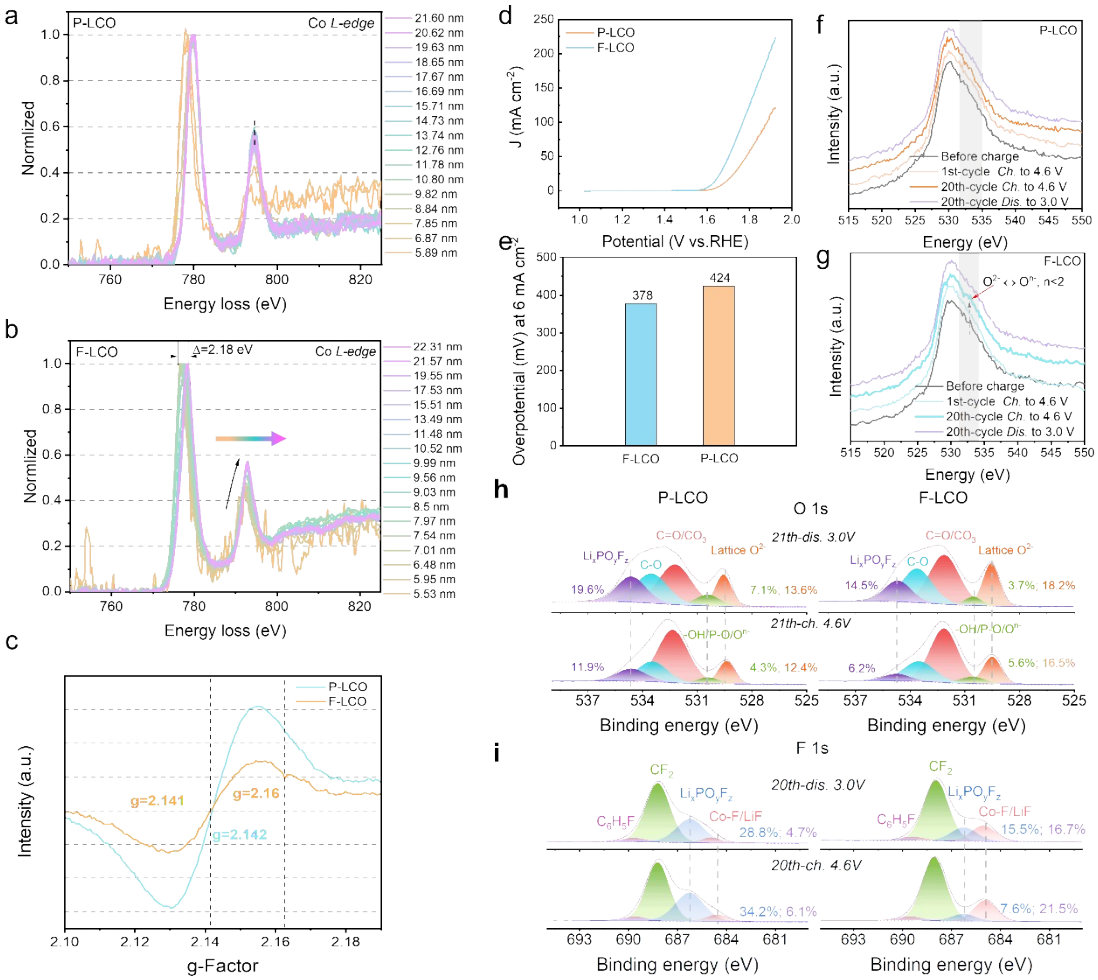

Supplementary Figure 20| Normalized EELS spectra of Co *L*-edge (a) P-LCO and (b) F-LCO. (c) Perpendicular-mode EPR spectra of P-LCO and F-LCO electrodes at powder state. (d-e) OER electrocatalytic performances of P-LCO and F-LCO in 1 M KOH aqueous solution at room temperature. (d) Linear sweep voltammetry (LSV) curves at a scan rate of 5 mV s^{-1}. Potentials are *vs.* reversible hydrogen electrode (RHE). (e) Measured overpotential at 6 mA cm^{-2} current density. (f-g) O K-edge SXAS spectra of (f) P-LCO and (g) F-LCO in different states of charge under TEY modes. (h-i) XPS analysis of (h) O 1s and (i) F 1s for P-LCO and F-LCO cathodes under 0.2 C charge/discharge state after 20 cycles.

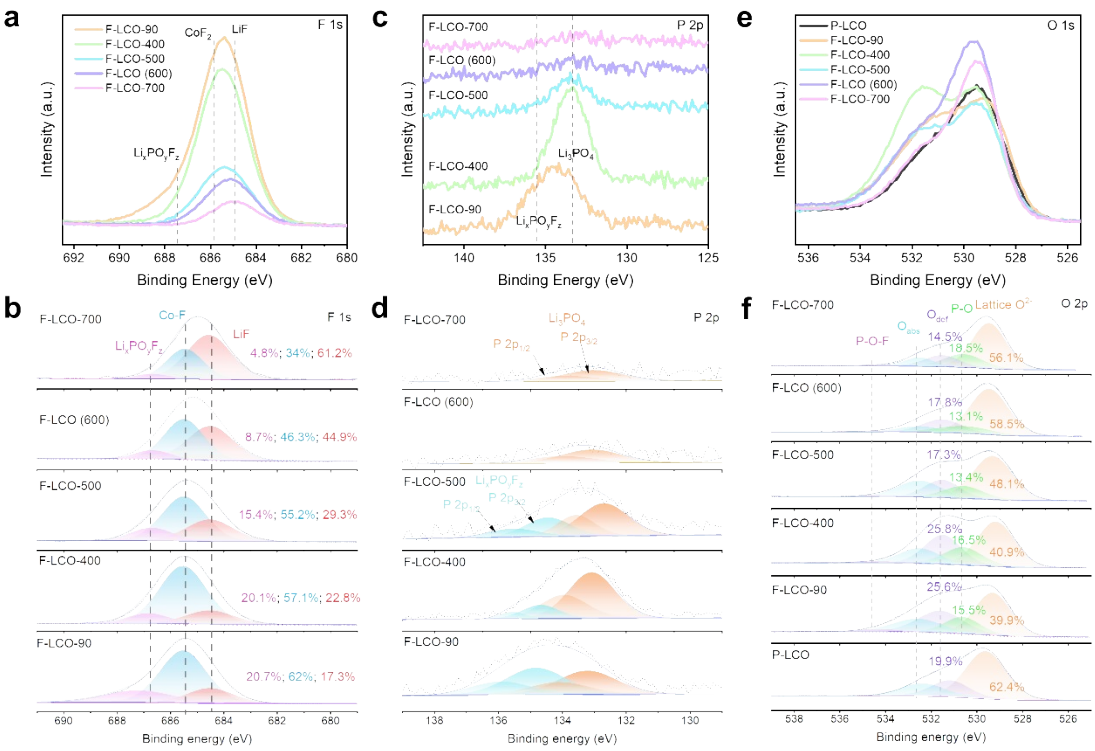

Supplementary Figure 21| XPS analysis of (a-b) F 1s, (c-d) P 2p, and (e-f) O 1s for different LCO cathodes.

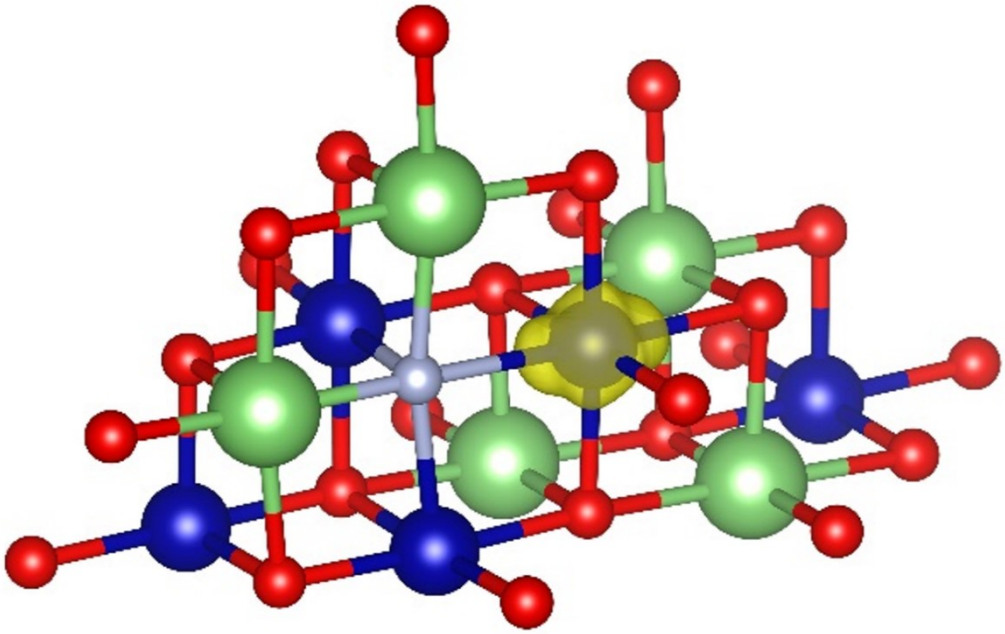

Supplementary Figure 22| Spin density of LCO bulk with one substituted F atom. Spin-polarized area is represented by yellow color.

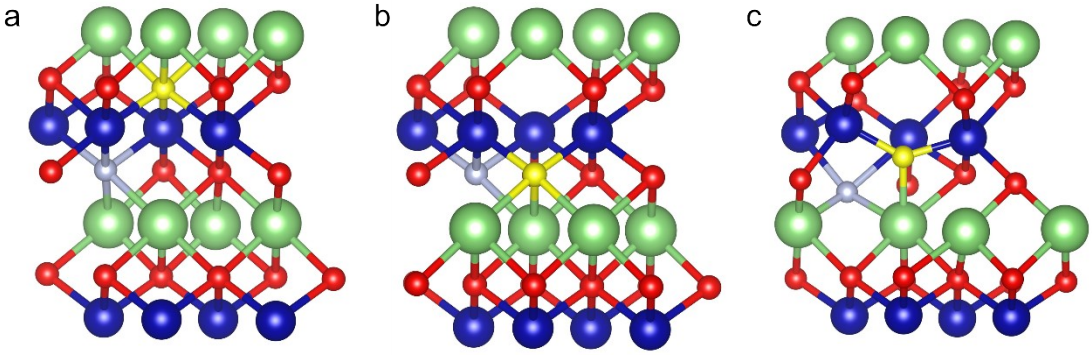

Supplementary Figure 23| Diffusion pathway of O atom in bulk LCO with one substituted F atom. (a) Initial state, (b) transition state, and (c) final state are depicted with Li, O, Co, and F atoms represented by green, red, blue, and light blue spheres, respectively. The diffused O atom is represented by the yellow sphere.

Supplementary Table S1. Performance comparison of cycling performance of our F-LCO with the reported 4.6 V LCO cathodes (*vs.* Li^+/Li).

Modification strategy	Rate ($C/mA\ g^{-1}$)	Capacity	Retention	Refs.
Hydrothermal assisted Li/Al/F- modified LCO	27.4	171 mA h g^{-1} after 200 cycles	82.2% after 200 cycles	5
Ti/Al/Mg co-doped LCO	137	174 mA h g^{-1} after 100 cycles	86% after 100 cycles	6
Al/Ti bulk-doped and Mg surface-doped LCO	137	170 mA h g^{-1} after 200 cycles	80.2% after 200 cycles	7
$LiMn_{1.5}Ni_{0.5}O_4$ coated LCO	50	182 mA h g^{-1} after 100 cycles	80.0% after 200 cycles	8
AlZnO coated LCO	185	121 mA h g^{-1} after 500 cycles	65.7% after 500 cycles	9
LATP coated LCO	137	180 mA h g^{-1} after 100 cycles	85.8% after 100 cycles	10
P/Ni co-doped LCO	137	188 mA h g^{-1} after 100 cycles	92.6% after 100 cycles	11
Se surface-doped LCO	70	189 mA h g^{-1} after 120 cycles	86.7% after 120 cycles	12
Trace SO_2 in-situ modified LCO	280	176 mA h g^{-1} after 100 cycles	88% after 100 cycles	13
Al and F gradient-doped LCO	100	170.8 mA h g^{-1} after 200 cycles	86.9% after 200 cycles	14
Li-Al-PO_4 coated LCO	137	180.4 mA h g^{-1} after 200 cycles	88.6 after 200 cycles	15
$LiAlH_4$ treated LCO	190	143.7 mA h g^{-1} after 500 cycles	71.6% after 500 cycles	16
Co_xB_y coated Mg-doped LCO	27 0	185.5 mA h g^{-1} after 100 cycles	94.6% after 100 cycles	17
Mg^{2+} and $(PO_4)^{3-}$ co-doped LCO	270	137.5 mA h g^{-1} after 100 cycles	82.4% after 1000 cycles	18
LiCoPO4 coated LCO	2C/400	153 mA h g^{-1} after 1000 cycles	75% after 1000 cycles	19
MgF_2 doped LCO	5C/1350	130 mA h g^{-1} after 1000 cycles	86.4% after 1000 cycles	20
V-doped LCO	5C/1350	110 mA h g^{-1} after 200 cycles	93.4% after 200 cycles	21
Se coated Mg-doped LCO	2C/400	128 mA h g^{-1} after 1000 cycles	68.5% after 1000 cycles	22

	for charge and 5C/1000 for discharge			
Lathurized LCO	5C/1000	170 mA h g^{-1} after 600 cycles,	89.4% after 600 cycles,	23
F-LCO	3C/822	167 mA h g^{-1} after 100 cycles 165 mA h g^{-1} after 300 cycles 162 mA h g^{-1} after 500 cycles 159 mA h g^{-1} after 700 cycles 155 mA h g^{-1} after 1000 cycles	99.0% after 100 cycles, 96.0% after 300 cycles, 94.3% after 500 cycles, 94.3% after 700 cycles, 91.9% after 1000 cycles	This work

Supplementary Table S2. Doping element composition of commercial P-LCOs from ICP-OES.

Doping elements	Proportions (mol%)
Ti	4.59
Mg	0.16
Al	0.61
B	0.57

Supplementary references

1. G. K. a. J. Furthmüller, *Phys. Rev. B: Condens. Matter Mater. Phys.,*, 1996, **54**, 11169–11186.
2. K. B. a. M. E. J. P. Perdew, *Phys. Rev. Lett.*, 1996, **77**, 3865-3868.
3. P. E. Blüochl, *Phys. Rev. B: Condens. Matter Mater. Phys.*, 1994, **50**, 17953-17979.
4. C. L. Sun, X. B. Liao, F. J. Xia, Y. Zhao, L. Zhang, S. Mu, S. S. Shi, Y. X. Li, H. Y. Peng, G. Van Tendeloo, K. N. Zhao and J. S. Wu, *ACS Nano*, 2020, **14**, 6181-6190.
5. J. Qian, L. Liu, J. Yang, S. Li, X. Wang, H. L. Zhuang and Y. Lu, *Nat. Commun.*, 2018, **9**, 4918.
6. J.-N. Zhang, Q. Li, C. Ouyang, X. Yu, M. Ge, X. Huang, E. Hu, C. Ma, S. Li, R. Xiao, W. Yang, Y. Chu, Y. Liu, H. Yu, X.-Q. Yang, X. Huang, L. Chen and H. Li, *Nat. Energy*, 2019, **4**, 594-603.
7. L. Wang, J. Ma, C. Wang, X. Yu, R. Liu, F. Jiang, X. Sun, A. Du, X. Zhou and G. Cui, *Adv. Sci.*, 2019, **6**, 1900355.
8. Z. Zhu, D. Yu, Z. Shi, R. Gao, X. Xiao, I. Waluyo, M. Ge, Y. Dong, W. Xue, G. Xu, W.-K. Lee, A. Hunt and J. Li, *Energy Environ. Sci.*, 2020, **13**, 1865-1878.
9. T. Cheng, Z. T. Ma, R. C. Qian, Y. T. Wang, Q. Cheng, Y. C. Lyu, A. M. Nie and B. K. Guo, *Adv. Funct. Mater.*, 2021, **31**, 2001974.
10. Y. Wang, Q. Zhang, Z. C. Xue, L. Yang, J. Wang, F. Meng, Q. Li, H. Pan, J. N. Zhang, Z. Jiang, W. Yang, X. Yu, L. Gu and H. Li, *Adv. Energy Mater.*, 2020, **10**, 2001413.
11. N. Qin, Q. Gan, Z. Zhuang, Y. Wang, Y. Li, Z. Li, H. Iftikhar, C. Zeng, G. Liu, Y. Bai, K. Zhang and Z. Lu, *Adv. Energy Mater.*, 2022, **12**, 2201549.
12. Z. Zhu, H. Wang, Y. Li, R. Gao, X. Xiao, Q. Yu, C. Wang, I. Waluyo, J. Ding, A. Hunt and J. Li, *Adv. Mater.*, 2020, **32**, e2005182.
13. X. Tan, T. Zhao, L. Song, D. Mao, Y. Zhang, Z. Fan, H. Wang and W. Chu, *Adv. Energy Mater.*, 2022, **12**, 2200008.
14. W. Huang, Q. Zhao, M. Zhang, S. Xu, H. Xue, C. Zhu, J. Fang, W. Zhao, G. Ren, R. Qin, Q. Zhao, H. Chen and F. Pan, *Adv. Energy Mater.*, 2022, **12**, 2200813.
15. X. Wang, Q. Wu, S. Li, Z. Tong, D. Wang, H. L. Zhuang, X. Wang and Y. Lu, *Energy Storage Mater.*, 2021, **37**, 67-76.
16. P. Wang, Y. Meng, Y. Wang, L. Chen, Z. Zhang, W. Pu, J. Li, C. Yang and D. Xiao, *Energy Storage Mater.*, 2022, **44**, 487-496.
17. J. Chen, H. Chen, S. Zhang, A. Dai, T. Li, Y. Mei, L. Ni, X. Gao, W. Deng, L. Yu, G. Zou, H. Hou, M. Dahbi, W. Xu, J. Wen, J. Alami, T. Liu, K. Amine and X. Ji, *Adv. Mater.*, 2022, **34**, 2204845.
18. W. Kong, D. Zhou, Q. Zhang, D. Wong, K. An, C. Schulz, N. Zhang, J. Zhang and X. Liu, *Adv. Funct. Mater.*, 2022, **33**, 2211033.
19. X. R. Yang, C. W. Wang, P. F. Yan, T. P. Jiao, J. L. Hao, Y. Y. Jiang, F. C. Ren, W. G. Zhang, J. M. Zheng, Y. Cheng, X. S. Wang, W. Yang, J. P. Zhu, S. Y. Pan, M. Lin, L. Y. Zeng, Z. L. Gong, J. T. Li and Y. Yang, *Adv. Energy Mater.*, 2022, **12**, 2200197.
20. W. Kong, J. Zhang, D. Wong, W. Yang, J. Yang, C. Schulz and X. Liu, *Angew. Chem., Int. Ed.*, 2021, **60**, 27102-27112.
21. W. J. Kong, D. Wong, K. An, J. C. Zhang, Z. H. Chen, C. Schulz, Z. J. Xu and X. F. Liu, *Adv. Funct. Mater.*, 2022, **32**, 2202679.
22. A. Fu, Z. Zhang, J. Lin, Y. Zou, C. Qin, C. Xu, P. Yan, K. Zhou, J. Hao, X. Yang, Y. Cheng, D.-

Y. Wu, Y. Yang, M.-S. Wang and J. Zheng, *Energy Storage Mater.*, 2022, **46**, 406-416.

23. M. Z. Cai, Y. H. Dong, M. Xie, W. J. Dong, C. L. Dong, P. Dai, H. Zhang, X. Wang, X. Z. Sun, S. N. Zhang, M. Yoon, H. W. Xu, Y. S. Ge, J. Li and F. Q. Huang, *Nat. Energy*, 2023, **8**, 159-168.